

The dispersal of protoplanetary discs. – II: Photoevaporation models with observationally derived irradiating spectra

Barbara Ercolano^{1,2*}, Giovanni Picogna¹, Kristina Monsch^{1,3}, Jeremy J. Drake³,
Thomas Preibisch¹

¹ *Universitäts-Sternwarte, Fakultät für Physik, Ludwig-Maximilians-Universität München, Scheinerstr. 1, 81679 München, Germany*

² *Exzellenzcluster ‘Origins’, Boltzmannstr. 2, 85748 Garching, Germany*

³ *Smithsonian Astrophysical Observatory, 60 Garden Street, Cambridge MA02138, USA*

10 September 2021

ABSTRACT

Young solar-type stars are known to be strong X-ray emitters and their X-ray spectra have been widely studied. X-rays from the central star may play a crucial role in the thermodynamics and chemistry of the circumstellar material as well as in the atmospheric evolution of young planets. In this paper we present model spectra based on spectral parameters derived from the observations of young stars in the Orion Nebula Cluster from the *Chandra* Orion Ultradeep Project (COUP). The spectra are then used to calculate new photoevaporation prescriptions that can be used in disc and planet population synthesis models. Our models clearly show that disc wind mass loss rates are controlled by the stellar luminosity in the soft (100 eV–1 keV) X-ray band. New analytical relations are provided for the mass loss rates and profiles of photoevaporative winds as a function of the luminosity in the soft X-ray band. The agreement between observed and predicted transition disc statistics moderately improved using the new spectra, but the observed population of strongly accreting large cavity discs can still not be reproduced by these models. Furthermore, our models predict a population of non-accreting transition discs that are not observed. This highlights the importance of considering the depletion of millimeter-sized dust grains from the outer disc, which is a likely reason why such discs have not been detected yet.

Key words: protoplanetary discs, winds, photoevaporation

1 INTRODUCTION

Thermal and magnetic winds are thought to play a crucial role in the evolution of protoplanetary discs (e.g. [Ercolano & Pascucci 2017a](#); [Alexander et al. 2014](#)). In particular, observations suggest that the final dispersal of the disc material must occur quickly and proceed from the inside-out (e.g. [Koeperl et al. 2013](#); [Ercolano et al. 2015](#); [Luhman et al. 2010](#); [Ercolano et al. 2011](#)). Thermally unbound and centrifugally launched winds, known as photoevaporative winds, can easily reproduce this observed fast, inside-out dispersal, and in particular, X-ray-driven photoevaporative winds have been shown to produce mass loss rates

comparable to observed accretion rates on young low-mass stars ([Ercolano et al. 2009a](#); [Owen et al. 2010](#); [Picogna et al. 2019](#)). Also, a significant fraction of the so-called transition discs can be explained either by disc dispersal via photoevaporation alone ([Ercolano et al. 2018](#)) or in combination with magnetic fields ([Wang & Goodman 2017a](#)).

There is growing indirect evidence that X-rays from the central star may indeed be the major driver of photoevaporative winds (e.g. [Ercolano et al. 2014](#); [Monsch et al. 2019](#); [Flaischlen et al. 2021](#)), and these models can well reproduce some of the observed emission line diagnostics ([Ercolano & Owen 2010, 2016](#); [Weber et al. 2020](#)), although recent observations point to the presence of additional emission components which might also be attributed to magnetic disc winds

* E-mail: ercolano@usm.lmu.de

L_X (erg/s)	T_1 (10^6 K)	T_2 (10^6 K)	EM_2/EM_1	model name
10^{29}	8	22	0.6	Spec29
10^{30}	9	30	1.6	Spec30
10^{31}	10	35	2.5	Spec31

Table 1. Mean spectral parameters from two-component temperature fits of some 500 X-ray spectra of T Tauri stars in the COUP data. T_1 and T_2 correspond to the temperatures of the “cool” and “hot” plasma components, respectively, while EM_2/EM_1 indicates the ratio of the corresponding emission measures. The spectral hardness increases with increasing X-ray luminosity.

(e.g. Pascucci et al. 2020; Banzatti et al. 2019; Nisini et al. 2018; Gangi et al. 2020).

Current X-ray photoevaporation models span the observed parameter space in X-ray luminosities (Picogna et al. 2019, hereafter Paper I), carbon depletion (Wölfer et al. 2019), and stellar masses (Picogna et al., in preparation). All of these models, however, use the same irradiating spectrum, namely the synthetic spectrum employed by Ercolano et al. (2008b, 2009a). Other studies, that employed different irradiating spectra in the X-ray domain have therefore yielded different conclusions as to the efficacy of X-rays to drive a photoevaporative wind. In particular, when using hard X-ray spectra with substantial flux at or above 1 keV, other authors have found that X-rays become inefficient at driving the wind (Wang & Goodman 2017b; Nakatani et al. 2018). This is not surprising as was shown by Ercolano et al. (2009b), who found that the soft X-ray band (< 1 keV) by far dominates the heating in the wind launching regions. While hard X-rays can penetrate larger columns of gas where the densities are much higher, they are nevertheless unable to provide enough heating in those regions to unbind the gas. Thus it is clear that a realistic X-ray spectrum is of crucial importance to determine the thermodynamics in the disc atmospheres. This affects the wind as well as the emission line spectrum emerging from the disc atmosphere and the wind (Schisano et al. 2010).

In this paper we use the results from the *Chandra* Orion Ultradeep Survey (COUP, cf. Getman et al. 2005) of young stars in the Orion nebula cluster to infer typical parameters of the X-ray spectrum. Synthetic spectra are then derived from these parameters and used as input for radiation-hydrodynamical simulations of photoevaporating discs. We derive mass loss rates and profiles and provide prescriptions for population synthesis codes. The effects of the new calculations on the evolution of the disc surface density as well as the formation of transition discs and the migration of planets is also explored.

The new input spectra are derived and described in Section 2, while in Section 3 we summarise the numerical methods employed in the paper. Our results are presented in Section 4. Finally, Section 5 contains a discussion and a brief summary of the conclusions of this work.

2 THE X-RAY SPECTRA OF T TAURI STARS

For the simulations in this study, we calculated X-ray spectra appropriate for T Tauri stars with different levels of X-ray activity. The spectral parameters for these models were based on the results of the COUP project, an 838 ksec long

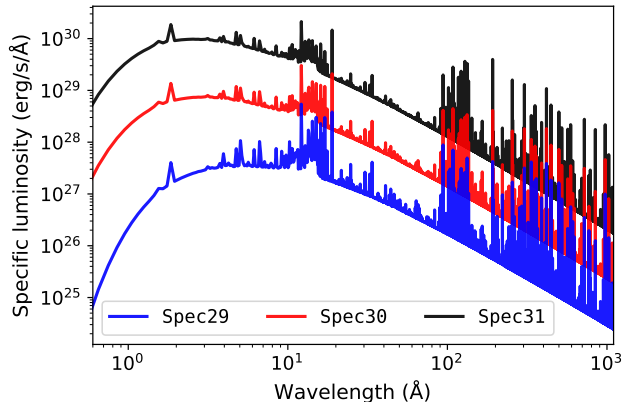


Figure 1. Synthetic spectra representative for the low-, medium- and high-X-ray luminous stars presented in this study, generated from observationally derived emission measures from the COUP data (cf. Section 2 and Table 1 for details).

Chandra observation of the Orion Nebula Cluster (ONC) and the deepest X-ray observation ever made of a young stellar cluster. The COUP data analysis showed that for the large majority of sources, the X-ray spectra could be well fitted by two-temperature thermal plasma models plus absorption. The resulting spectral parameters were thus: (a) the temperatures of the cool and hot plasma components, T_1 and T_2 , (b) the emission measures EM_1 and EM_2 of both components, and (c) the hydrogen column density for the foreground extinction (see Getman et al. 2005, for details of these parameters).

Preibisch et al. (2005) performed an analysis of the X-ray properties of the 598 optically visible likely ONC members that were detected as X-ray sources in the COUP data. This showed that the temperature of the cool plasma component (T_1) slightly increases with X-ray luminosity (or X-ray surface flux), while the hot plasma component (T_2) displays a stronger and clearer increase with X-ray luminosity (or X-ray surface flux). It was also found that the ratio of the emission measures, EM_2/EM_1 , systematically increases with the X-ray luminosity.

In order to cover the range of “typical” X-ray spectral properties for stars with different values of X-ray luminosity, we determined the typical values for T_1 , T_2 , and the ratio EM_2/EM_1 for three values of the X-ray luminosity, namely $\log(L_X/\text{erg s}^{-1}) = 29, 30, \text{ and } 31$ from the COUP data. These values are thus approximately representative of low-, medium- and high-X-ray luminous stars and thus cover the region in parameter space where the large majority of all T Tauri stars are located. This resulted in the values presented in Table 1.

Finally, we computed the X-ray spectra based on the plasma temperatures and relative emission measures shown in Figure 1 using the PINTofALE IDL software package¹ (Kashyap & Drake 2000) using spectral line and continuum emissivities computed from the CHIANTI database version 8.0.6. Spectra were then normalised to our adopted values of X-ray luminosity in the energy range of 0.5–5 keV.

¹ available at <https://hea-www.harvard.edu/PINTofALE/>.

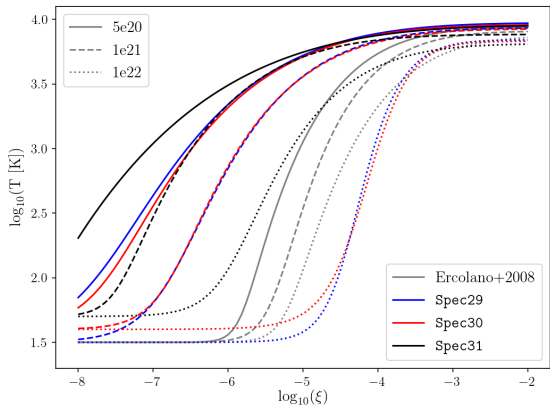


Figure 2. Temperature as a function of ionisation parameter for the X-ray spectrum of Ercolano et al. (2008b) shown in gray, compared to those derived in this work for $L_X = 10^{29} \text{ erg s}^{-1}$ (blue, Spec29), $L_X = 10^{30} \text{ erg s}^{-1}$ (red, Spec30), and $L_X = 10^{31} \text{ erg s}^{-1}$ (black, Spec31), for three representative column densities, $N = 5 \times 10^{20}, 1 \times 10^{21}$ and $1 \times 10^{22} \text{ cm}^{-2}$.

3 PHOTOEVAPORATION CALCULATION METHODS

We follow the approach of Owen et al. (2010, 2011, 2012) and Paper I, and perform 2D radiation-hydrodynamical calculations of primordial discs irradiated by a young central star to determine the steady-state solution for the photoevaporative flow. The total mass loss rate and the radial mass loss profiles are then obtained from the radiation-hydrodynamical calculations and used as a sink term in a 1D viscous evolution code, in order to predict the surface density evolution of the disc. The three main steps and codes used for each of these calculations are common with previous papers and are only briefly described in the next section, where the references to the more complete descriptions and validation of the methods are also given.

3.1 Thermal calculations

Wölfer et al. (2019) and Ercolano & Clarke (2010) showed that for the same ionisation parameter, $\xi = L_X/(nr^2)$ (where n is the volume number density and r is the spherical radius), column density N , and irradiation spectrum, the temperature of the gas is sensitive to the local elemental abundances. The irradiation spectrum, however, is also expected to influence the temperature of the gas. We thus follow Paper I and Wölfer et al. (2019) and use the photoionisation code MOCASSIN (Ercolano et al. 2003, 2005, 2008a) to determine parameterisations of the gas temperature as a function of the ionisation parameter for 40 different gas column densities between $5 \times 10^{20} \text{ cm}^{-2}$ to $2 \times 10^{22} \text{ cm}^{-2}$ for our new irradiating spectra. We refer to the previous work mentioned above for details about the MOCASSIN code (Ercolano et al. 2003, 2005, 2008a) and the elemental abundances used (Picogna et al. 2019), and only list the major heating and cooling channels included in the temperature equilibrium calculations in this work. Heating in the wind region and in the disc atmosphere is from photoionisation.

Dust photoelectric heating and dust-gas-collisions are included, but unimportant in these regions. Cooling is mainly via collisionally excited and recombination lines from abundant species. Other processes like free-free, Thomson and Compton scattering and two-photon continuum radiation are also included, but play a secondary role.

In Figure 2 we compare the temperature as a function of ionisation parameter for the X-ray spectrum of Ercolano et al. (2008b, 2009a) to those derived in this work for $L_X = 10^{29}, 10^{30}$, and $10^{31} \text{ erg s}^{-1}$ at three selected column densities of $N = 5 \times 10^{20}, 1 \times 10^{21}$ and $1 \times 10^{22} \text{ cm}^{-2}$. For column densities of $N \sim 5 \times 10^{20} \text{ cm}^{-2}$ up to the wind launching region of $N \sim 10^{22} \text{ cm}^{-2}$, the temperature at a given ξ is higher in our new parameterisations, compared to previous work of Picogna et al. (2019). This is mainly due to the fact that in the new spectra the fraction of energy coming out in the soft X-ray band (0.1 to 1 keV) is over a factor two higher than in the spectrum of Ercolano et al. (2008b, 2009a). Soft X-ray photons are most efficient at heating in this column density range. Local factors, including the specific cooling channels and the ionisation structure affecting may also play a role.

We describe the temperature prescription as a function of $\log \xi$, adopting a sigmoidal function as in Paper I:

$$\log T_e = d + \frac{a - d}{[1 + (\log \xi / c)^b]^m}, \quad (1)$$

where the parameters for the different column densities and spectra are given in Tables A1, A2, and A3 for the Spec29, Spec30 and Spec31 models, respectively.

3.2 2D Hydrodynamical calculations

We performed radiative-hydrodynamical simulations using a modified version of the PLUTO code (Mignone et al. 2007; Picogna et al. 2019), to accurately model the stellar irradiation. In the upper layers of the disc (i.e. in the column density range 5×10^{20} to $2 \times 10^{22} \text{ cm}^{-2}$), we adopted the parameterisation presented in the previous section, coming from the radiative transfer calculations in MOCASSIN. We linearly interpolated the temperatures for intermediate values of column densities and extrapolated the temperature for ionisation parameters outside the simulated range. The regions where these extrapolations were necessary were nevertheless circumscribed. For the bulk of the disc (i.e. column densities larger than $2 \times 10^{22} \text{ cm}^{-2}$), we assumed a perfect coupling between the gas and dust temperature, where the latter was mapped from the models of D’Alessio et al. (2001). For more details on the numerical implementation, see Paper I.

The numerical grid adopted was chosen to maximise the resolution close to the wind launching region. For this region we over-sampled the grid, adopting a static nested grid as summarised in Table 2. The hydrodynamical runs were started from the steady state solutions of Picogna et al. (2019) and then, once the new temperature prescription was applied, evolved for a few hundred orbits at 10 au until a new steady state in the flow was reached. In Figure 3, we show the gas density distribution for the three different cases, where the gas streamlines are overplotted at 5% interval steps of the cumulative mass loss rate.

variable	value
<i>disc extent</i>	
radial (au)	0.33–1000
polar (rad)	[0.01–0.5, 0.5–1.0, 1.0– $\pi/2$]
<i>grid resolution</i>	
radial	412
polar	[100, 200, 50]

Table 2. Input parameters for the 2D hydrodynamical models presented in Section 3.2.

The adopted X-ray luminosity has a strong impact on the disc flaring. For the same gas local properties and column densities, the gas temperature is higher for higher X-ray luminosity. Thus, the stellar irradiation can generate a thermal wind from deeper and denser regions in the disc. For high X-ray luminosities, we observe a flatter disc with a denser wind region, preventing the radiation from reaching the outermost parts of the disc. For low X-ray luminosities, the radiation is not able to heat the gas sufficiently to unbound it, and therefore the disc shows a larger flaring and a less dense wind. This allows the radiation to remove mass from a larger region of the disc, as one can infer from the resulting surface mass loss profile shown in Figure 4.

3.3 1D surface density calculations

The surface density evolution of a disc subject to viscosity and X-ray photoevaporation driven by the host star can be described by the following equation:

$$\frac{\partial \Sigma}{\partial t} = \frac{1}{R} \frac{\partial}{\partial R} \left[3R^{1/2} \frac{\partial}{\partial R} \left(\nu \Sigma R^{1/2} \right) \right] - \dot{\Sigma}_w(R, t), \quad (2)$$

where the first term describes the viscous evolution of the circumstellar disc (Lynden-Bell & Pringle 1974), and $\dot{\Sigma}_w(R, t)$ corresponds to the surface mass loss profile due to photoevaporation. Here, $\Sigma(R, t)$ describes the gas surface density, M_\star is the stellar mass, R the distance from the central star and G is the gravitational constant. In order to calculate the global evolution of the disc, we employed the 1D viscous evolution code SPOCK (Ercolano & Rosotti 2015) and discretised Eq. 2 on a grid of 1000 radial cells equispaced in $R^{1/2}$, which extends from 0.04 au to 10^4 au. The locally isothermal discs have an aspect ratio of $H/R = 0.1$ at R_1 , which results in flared discs following $H \propto R^{5/4}$, and a midplane temperature scaling as $T_{\text{mid}} \propto R^{-1/2}$, where $T_{\text{mid}} \approx [2100 \text{ K}, 4 \text{ K}]$ at the inner and outer boundary, respectively.

Considering a stellar mass of $M_\star = 0.7 M_\odot$ with an initial disc mass of $0.07 M_\odot$, we set $R_1 = 50$ au, which defines the exponential cutoff to the surface density and therefore sets the viscous timescale $t_\nu = R_1^2/(3\nu)$. The viscosity is defined as $\nu = \alpha c_s H$, where c_s is the sound speed of the gas, H the disc scale height and α the dimensionless Shakura-Sunyaev parameter (Shakura & Sunyaev 1973). In order to obtain observationally motivated lifetimes ranging from 3–10 Myr (e.g. Ribas et al. 2014, 2015) for discs subject to viscosity and X-ray photoevaporation, we chose $\alpha = 10^{-3}$.

Mass loss due to photoevaporation is implemented as a sink-term to the global surface density evolution of the disc, which removes a given amount of gas from each cell at

every timestep. The surface mass loss profile from Paper I is described by:

$$\dot{\Sigma}_w(R) = \ln 10 \left(\frac{6a \ln R^5}{R \ln 10^6} + \frac{5b \ln R^4}{R \ln 10^5} + \frac{4c \ln R^3}{R \ln 10^4} \right. \\ \left. + \frac{3d \ln R^2}{R \ln 10^3} + \frac{2e \ln R}{R \ln 10^2} + \frac{f}{R \ln 10} \right) \frac{\dot{M}_w(R)}{2\pi R}, \quad (3)$$

where

$$\dot{M}_w(R) = 10^{a \log R^6 + b \log R^5 + c \log R^4 + d \log R^3} \\ \times 10^{e \log R^2 + f \log R + g} \dot{M}_w(L_X), \quad (4)$$

and

$$\log \dot{M}_w(L_X) = a_L \exp \left(\frac{(\ln(\log L_X) - b_L)^2}{c_L} \right) + d_L, \quad (5)$$

with $a_L = -2.7326$, $b_L = 3.3307$, $c_L = -2.9868 \times 10^{-3}$ and $d_L = -7.2580$. The prefactors a to g are different for each irradiating spectrum, while the overall shape of the function describing the mass loss is mostly not affected, besides an exponential cut-off term that prevents any mass loss outside the radius R_{cut} , so that:

$$\dot{\Sigma}_{w,\text{hard}}(R) = \dot{\Sigma}_w(R) \exp \left[- \left(\frac{R}{R_{\text{cut}}} \right)^{10} \right]. \quad (6)$$

The corresponding prefactors and values of R_{cut} for each irradiating spectrum are given in Table 3. Figure 4 compares the resulting surface mass loss rate as a function of disc radius, obtained for the different irradiating spectra presented in this work to those of Paper I obtained with the spectra presented by Ercolano et al. (2008b, 2009a).

3.4 Giant planet migration calculations

As a next step, we expanded Eq. 2 in order to include the interaction of an embedded giant planet with its surrounding gaseous disc, which then reads:

$$\frac{\partial \Sigma}{\partial t} = \frac{1}{R} \frac{\partial}{\partial R} \left[3R^{1/2} \frac{\partial}{\partial R} \left(\nu \Sigma R^{1/2} \right) - \frac{2\Lambda \Sigma R^{3/2}}{(GM_\star)^{1/2}} \right] - \dot{\Sigma}_w(R, t). \quad (7)$$

The second term now treats the migration of the planet due to the specific angular momentum transfer from the planet to the disc, which is described by Λ .

We adopt the same approach as described in Ercolano & Rosotti (2015), but adjust the employed initial conditions in order to fit the different photoevaporation profiles in our study. Fully-formed planets of random mass between $0.5\text{--}5 M_J$ are inserted at 10 au into the disc and migrate inwards following the impulse approximation (Lin & Papaloizou 1979, 1986; Armitage et al. 2002, but see also Monsoch et al. 2021a). While the planets are allowed to accrete mass during their orbital evolution, their formation itself is not treated in our model. Therefore the insertion times of the planets were drawn randomly from a uniform distribution between 0.25 Myr and t_{clear} , where

$$t_{\text{clear}} = \frac{t_\nu}{3} \left(\frac{3M_d}{2t_\nu \dot{M}_w} \right)^{2/3}, \quad (8)$$

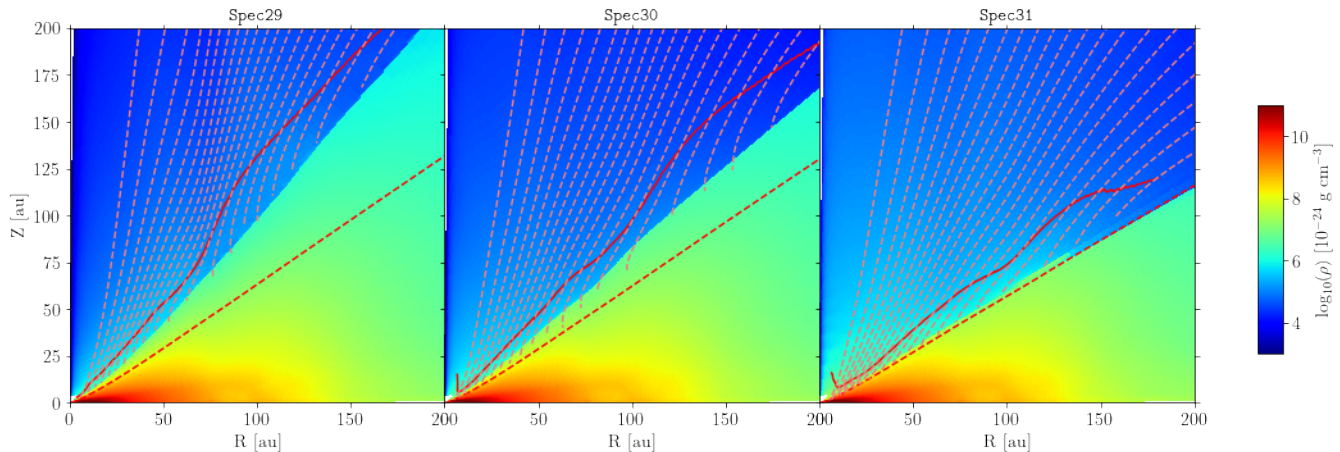


Figure 3. Density distribution at equilibrium for the different spectra. From left to right: *Spec29*, *Spec30*, *Spec31*. The solid red line shows the sonic surface, while in dashed red is plotted the maximum penetration depth of X-rays, and in dashed orange the gas streamlines every 5% of the cumulative mass loss rate.

parameter	Paper I	Spec29	Spec30	Spec31
a	-0.5885	-0.9152	0.3034	-1.2845
b	4.3130	8.5032	-1.5323	9.3601
c	-12.1214	-32.0623	1.5766	-27.7371
d	16.3587	62.8336	4.0211	42.9367
e	-11.4721	67.9150	-11.1311	-37.3244
f	5.7248	39.2652	10.6550	8.8216
g	-2.8562	-10.1113	-4.5769	-5.3780
R_{cut} (au)	120.	206.	105.	69.
\dot{M}_w (M_{\odot}/yr)	cf. Eq. 5	7.0×10^{-9}	3.9×10^{-8}	1.3×10^{-7}

Table 3. Parameterisation for the surface mass loss profile described by Eq. 3 and the resulting wind-mass loss rates for the different irradiating stellar spectra modelled in our study.

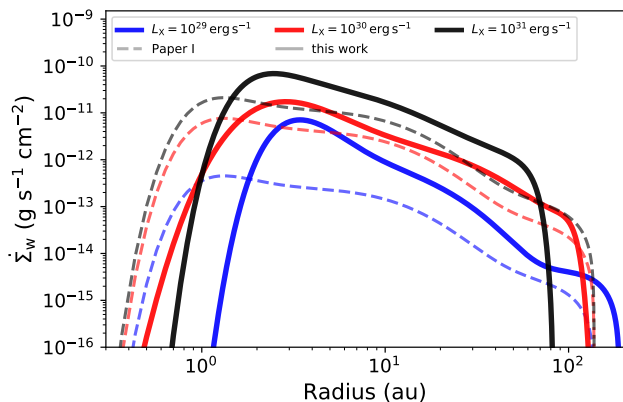


Figure 4. Surface mass loss rate as a function of disc radius obtained for the different irradiating spectra summarised in Table 3. The solid lines show the results for the *Spec29* (blue), *Spec30* (red) and *Spec31* (black) spectrum presented in this work. The dashed lines show the results for the X-ray input spectrum of [Ercolano et al. \(2008c, 2009b\)](#), which was used in [Paper I](#), evaluated for the same X-ray luminosities.

is the time at which photoevaporation starts to clear the disc ([Clarke et al. 2001](#); [Ruden 2004](#)). The lower limit of 0.25 Myr was chosen arbitrarily in order to provide a reasonable amount of time to form a giant planet following the core accretion paradigm ([Pollack et al. 1996](#)).

We ran in total 1000 simulations, for which L_X was sampled linearly between $\log(L_X/\text{erg s}^{-1}) = 28.5\text{--}31.5$. To account for the different surface mass loss profiles from the different irradiating spectra, this X-ray luminosity range was divided into three bins with $\log(L_X/\text{erg s}^{-1}) = [28.5\text{--}29.5, 29.5\text{--}30.5, 30.5\text{--}31.5]$, in which the corresponding surface mass loss profile (as given by Eq. 6 and Table 3) was used. Finally, the linearly sampled values of the X-ray luminosities were weighted following the X-ray luminosity function (XLF) of the COUP sample for pre-main sequence stars of $0.5 M_{\odot} \leq M_{\star} \leq 0.9 M_{\odot}$ ([Preibisch et al. 2005](#)). This step is necessary in order to obtain a realistic distribution of X-ray luminosities in our model, as otherwise the linear sampling of $\log L_X$ would introduce biased distributions especially towards lower values of the X-ray luminosity.

4 RESULTS

In this section we discuss the effects of our updated irradiating spectrum on specific aspects of disc evolution. In particular, we focus on (a) the global mass loss rates and the radial mass loss profiles obtained from the steady state 2D hydrodynamic calculations, (b) the global one dimensional evolution of the disc surface density and (c) the final orbital distribution of giant planets in discs.

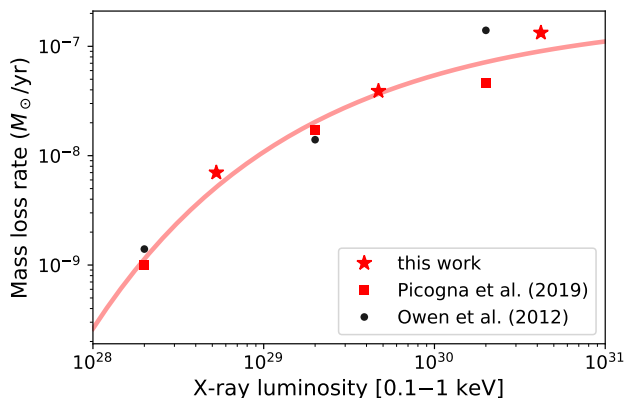


Figure 5. Wind mass loss rate as a function of X-ray luminosity integrated between 100 eV to 1 keV. Red stars show the values for the cumulative mass loss rates determined for the `Spec29`, `Spec30` and `Spec31` models, respectively, which are summarised in Table 3. Red squares are the corresponding values for the spectrum used in Paper I. The red line shows an appropriate fit for all red data points, which is given by Eq. 9. For comparison, the mass loss rates from Owen et al. (2012), computed within the same spectral range, are overplotted as well.

4.1 Mass loss rates and profiles

The global mass loss rates obtained in this work are quantitatively compared in Table 4 to the ones obtained by Paper I for the same disc configuration, but the spectrum of Ercolano et al. (2008b, 2009a). The differences reported in Table 4 are driven by the differences in the integrated luminosity in the ‘soft’ X-ray band (0.1–1 keV) of the spectrum, which are also reported in the same table. Figure 5 shows the resulting values for the cumulative mass loss rate $\dot{M}_w(L_{X,\text{soft}})$ both from this study and Paper I as a function of the integrated X-ray luminosity within the 0.1–1 keV spectral band. The relation for $\dot{M}_w(L_X)$ given by Owen et al. (2012), integrated within the same spectral band, is overplotted for comparison.

When plotted against the luminosity in the ‘soft’ X-ray region, both sets of simulations agree to within factors of a few (see Figure 5). We thus find that the mass loss rates integrated over the whole disc are not very sensitive to reasonable changes in the input spectrum, i.e. within the ranges of the observed X-ray output of the central stars.

We provide an updated \dot{M}_w parameterisation in terms of $L_{X,\text{soft}}$ [0.1–1 keV], which can be used in population synthesis models to better describe the wind mass loss rates for different stellar irradiating spectra. This is shown as the red line in Figure 5, which uses the same fitting function as given by Eq. 5:

$$\log \dot{M}_w(L_{X,\text{soft}}) = a_L \exp\left(\frac{(\ln(\log L_{X,\text{soft}}) - b_L)^2}{c_L}\right) + d_L, \quad (9)$$

however now with changed prefactors of $a = -1.947 \times 10^{17}$, $b = -1.572 \times 10^{-4}$, $c = -2.866 \times 10^{-1}$ and $d = -6.694$.

These results suggest that reasonable estimates of the total wind mass loss rates for different input X-ray spectra can be obtained by computing the integrated input flux in the 0.1–1 keV spectral band and applying the simple analyt-

$\log(L_X/\text{erg s}^{-1})$	29	30	31
\dot{M}_w [$10^{-8} M_\odot \text{ yr}^{-1}$]			
Paper I	0.10	1.7	4.6
This Work	0.70	3.9	13.3
disc lifetime [Myr]			
Paper I	19.4	2.7	1.2
This Work	13.1	1.6	0.7
Time of gap opening [% of t_{disc}]			
Paper I	79	75	72
This Work	76	69	43
$L_{X,\text{soft}}$ [$10^{29} \text{ erg s}^{-1}$]			
Paper I	0.2	2.0	20.
This Work	0.53	4.7	42.

Table 4. Total mass loss rates in the wind, global disc lifetime and luminosity of the input spectrum between 0.1–1 keV. The global disc lifetime was obtained assuming a disc of initial mass of $0.07 M_\odot$, a disc scaling radius of $R_1 = 50 \text{ au}$ and $\alpha = 10^{-3}$.

ical formula above. Our models therefore confirm the suggestion of Ercolano et al. (2009a) that the soft X-ray band is most efficient at driving the bulk of the photoevaporative wind.

It follows from Figure 4 that the radial extent of the surface mass loss profile decreases for larger X-ray luminosities. As discussed in Section 3.2, this is due to the fact that for high X-ray luminosities the wind in the inner region screens the outer disc region, preventing their irradiation, when diffuse fields are neglected. As a result, the disc scale height at large radii is much smaller for high X-ray luminosities and the mass loss profile is less extended. This can be more quantitatively assessed by comparing the R_{cut} parameter listed in Table 3, which is 69 au for $L_X = 10^{31} \text{ erg s}^{-1}$, 105 au for $L_X = 10^{30} \text{ erg s}^{-1}$ and 120 au for $L_X = 10^{29} \text{ erg s}^{-1}$. In comparison, R_{cut} stays constant at roughly 120 au for all three L_X cases when using the same spectrum as in Paper I. This demonstrates that the variation of R_{cut} is driven by the variation in spectral hardness rather than the simple variation of L_X .

This effect also explains the flattening of the mass loss rate to X-ray luminosity relation for high values of the X-ray luminosities (Figure 5), which was already reported in Paper I. This occurs since $\dot{M}_w \propto \int \dot{\Sigma}_w(R) R^2 dR$, thus mass loss in the outer parts of the disc carries a larger contribution to the total mass loss rate.

4.2 Evolution of the disc surface density

In this section we explore the global evolution of the surface density of discs subjected to irradiation from the different spectra shown in Figure 1.

In Figure 6 the surface density as a function of disc radius is plotted at several time steps of the total disc lifetime, t_{disc} , for the three spectra used in this work (right columns) and compared to previous calculations by Paper I (left columns). The red lines show the corresponding mass loss profile and the black lines show the surface density of the disc between [0, 50, 70, 75, 76, 80, 85, 90, 95, 99] % of the corresponding total disc lifetime. This is defined as the time in which the maximum surface density within the disc becomes less than 0.1 g cm^{-2} or once the disc reaches a maximum age of 10 Myr, as is the case in the upper left panel,

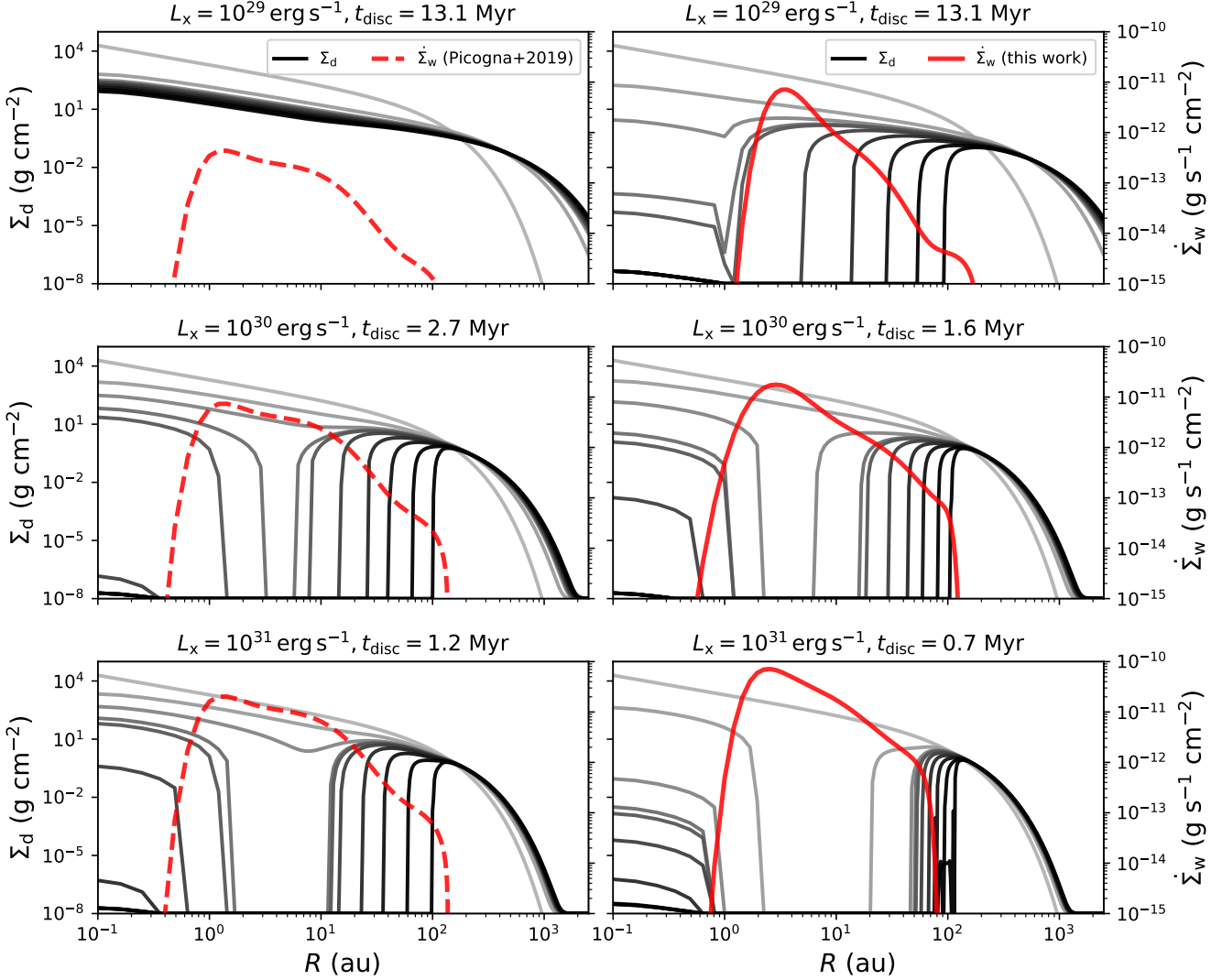


Figure 6. Comparison of the surface density evolution of a disc with initial mass of $M_d = 0.07 M_\odot$, $R_1 = 50$ au, $\alpha = 10^{-3}$ using the different input spectra for the X-ray luminosity bins for the calculation of the surface mass loss profile (see Eq. 3). The temporal evolution of the disc surface density (Σ_d) was plotted at [0, 50, 70, 75, 76, 80, 85, 90, 95, 99] % of the corresponding, total disc lifetime, starting from the lightest grey line and with darker grey lines indicating increasing age.

at which the simulation was forced to stop before the disc could be fully dispersed.

When compared to Paper I, the surface density evolution of the disc does not appear to be significantly sensitive to the choice of an observationally-motivated input spectrum. The gap opens roughly at the same location (i.e. between 2–3 au) and rapidly widens, as the inner disc drains viscously and the outer disc is dispersed away by the photoevaporative flow, powered by direct irradiation. While the broad-brush picture is roughly unchanged, there are differences in the global disc lifetimes and in the time at which the gap opens, as can be seen from the values reported in Table 4. These differences can be explained by the fact that we are comparing models that have the same integrated X-ray luminosity, but a different spectral hardness, thus resulting in different luminosities in the soft X-ray band ($L_{x,\text{soft}}$) in Table 4.

4.3 Population synthesis: transition disc statistics and giant planet distributions

Photoevaporation prescriptions play an important role in population synthesis models of protoplanetary discs (e.g. Owen et al. 2011; Ercolano et al. 2018; Picogna et al. 2019) as well as planet formation (Manara et al. 2019) and migration (Ercolano & Rosotti 2015; Jennings et al. 2018; Monsch et al. 2021a). In what follows, we explore whether one can expect appreciable differences in population syntheses of both transition discs or planet migration, by comparing the photoevaporation prescriptions from this work to those of Paper I, using very simple set-ups.

4.3.1 Transition disc statistics

Transition discs, i.e. discs which present an inner cavity depleted of dust, can be formed via several pathways. Giant

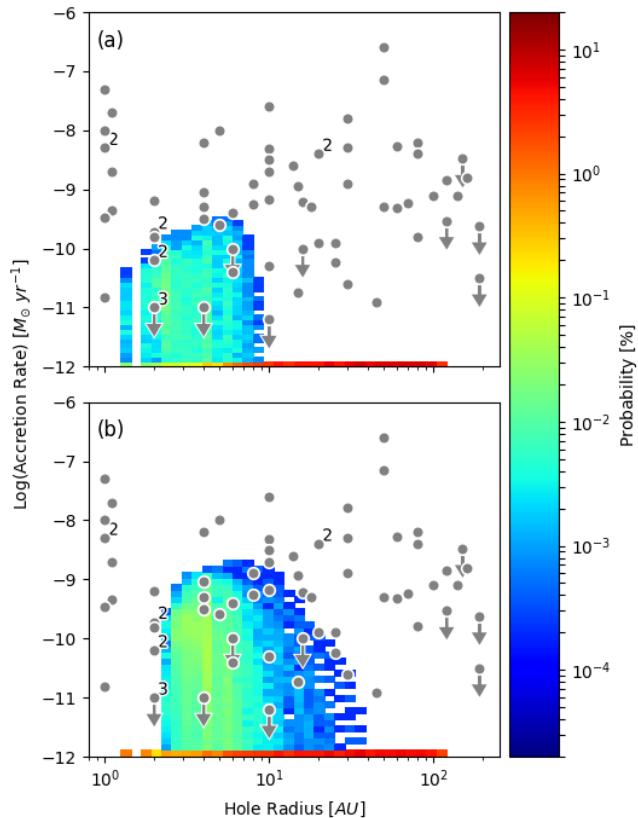


Figure 7. Transition disc demographics of our synthetic populations. The grey circles show observed transition discs from the collection of [Ercolano & Pascucci \(2017b\)](#). Numbers next to the circles indicate the total number of sources at that point, arrows indicate that the accretion rate is an upper limit. The coloured areas show the probability of finding a transition disc with the corresponding accretion rate and hole radius, calculated from populations of our X-ray driven photoevaporating disc models. Discs with an accretion rate lower than $10^{-12} M_{\odot} \text{ yr}^{-1}$ are shown at the bottom. Panel (a) shows the results for the disc population adopting the old spectra from [Paper I](#), panel (b) shows the results from the new spectra presented in this work.

planet formation and inside-out dispersal from photoevaporative winds are two of the leading theories to explain observations. The observed population of transition discs span a large range of central cavity sizes and accretion rates onto the central star. While photoevaporative models are more suited to explain lower rate accretors with small gap sizes, the opposite regime is often associated with the presence of an embedded planet. A combination of photoevaporation and supersonic accretion powered by magnetic fields has also been proposed to explain objects with large cavities and large accretion rates, that are difficult to explain otherwise ([Wang & Goodman 2017a](#)). Alternatively, vigorous photoevaporative winds acting in carbon-depleted discs could also help explaining this type of objects ([Wölfer et al. 2019](#)).

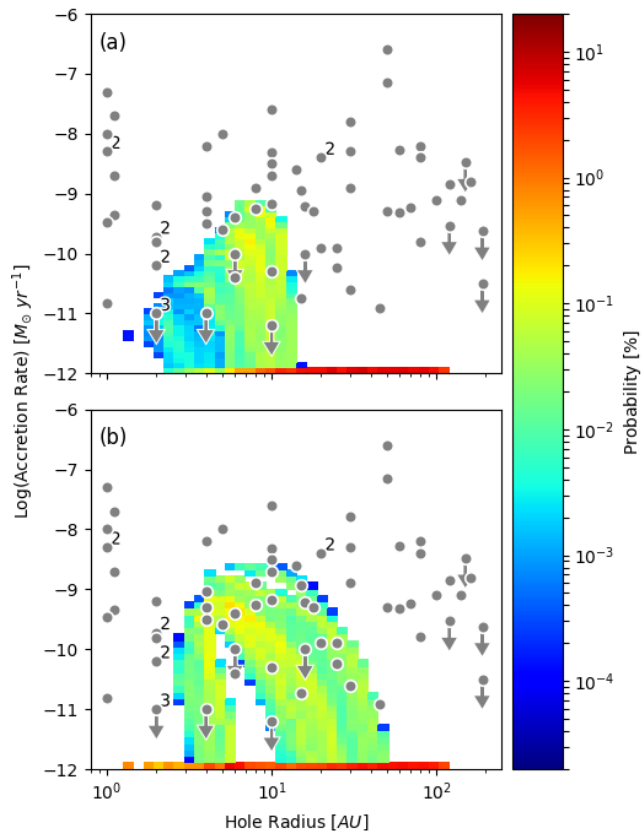


Figure 8. Same as [Figure 7](#) but with the initial value of R_1 randomly sampled as described in [Ercolano et al. \(2018\)](#) and the α value chosen in order to retain a disc lifetime consistent with the observed disc population.

In order to understand what fractions of the observed population can be explained by photoevaporation, and what is the influence of the improved spectra presented in this paper, we ran a disc population synthesis (see [Figure 7](#)), where we compared our new results (panel b) with those coming from the spectra used in [Paper I](#) (panel a). The colour-coding shows the probability of finding a given object at the corresponding accretion rate and hole radius. Due to high amount of objects with low accretion rates and large hole radii, the probability of all remaining objects is considerably low. This can be considered as an artefact of our numerical model and will be discussed in more detail later. The new spectra are able to cover larger fractions of the observed transition disc population (24.4% vs. 14.6%), by extending the covered part of the plot both towards higher accretion rates ($> 10^{-9} M_{\odot}/\text{yr}$), and larger cavity radii (~ 40 au).

[Figure 7](#) was obtained adopting a fixed value of the α -viscosity for all discs. Choosing a randomly sampled disc scaling radius and adapting the value of α in order to match the observed disc lifetimes (see [Ercolano et al. 2018](#), for details), we obtain the populations plotted in [Figure 8](#), which

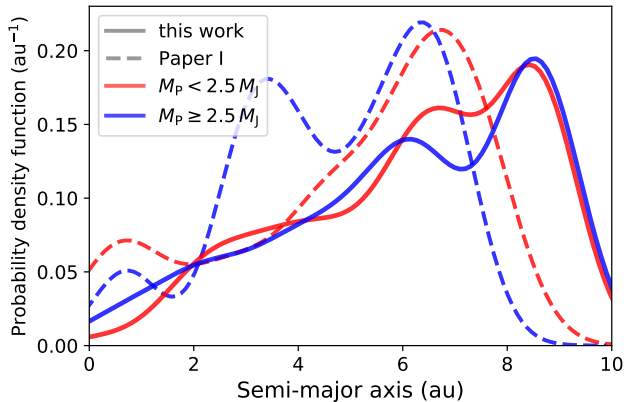


Figure 9. Kernel density estimate for the semi-major axis distribution resulting from the population synthesis models described in Sect. 4.3.2. The models assumed discs with $M_d = 0.07 M_\odot$, $R_1 = 50$ au and $\alpha = 10^{-3}$. The red lines show the low-mass giant planet population ($M_p < 2.5 M_J$), and the blue lines correspond to the high-mass one ($M_p \geq 2.5 M_J$). The distributions shown as dashed lines follow from the model using the photoevaporation profile as described by Paper I, while the solid lines use the photoevaporation profiles presented in this study.

show an increased probability of observing accreting transition discs.

Both approaches, however, still fall short of explaining the population of strongly accreting discs with large cavities and further strongly over-predict non-accreting transition discs (so-called ‘relic discs’). We note, however, that our models only deal with the evolution of the gas phase and it is thus unclear whether the relic discs that are over-produced in our models would actually be observable in the mm-continuum. Indeed, radial drift may have already removed most large grains from the outer regions of these discs by the time the cavity is opened, thus rendering these discs de-facto invisible (Ercolano et al. 2017). Population syntheses that self-consistently consider dust evolution within the discs are needed to explore this avenue. While these are beyond the scope of this paper, they are the subject of future work.

Finally, it is becoming increasingly clear that magneto-hydrodynamic (MHD) winds may also play an important part in the evolution of the surface density of discs, particularly at earlier times (e.g. Kunitomo et al. 2020). Our models do not account for this potentially important component which may have an effect on the resulting population synthesis of transition discs.

4.3.2 Giant planet distributions

Figure 9 shows the results of a planet population synthesis using the same approach as previously described in Ercolano & Rosotti (2015) and Monsch et al. (2021b). The figure shows the semi-major axis distribution of the planet population synthesis models, calculated using a Gaussian kernel density estimate. The red lines show the low-mass giant planet population ($M_p < 2.5 M_J$), and the blue lines correspond to the high-mass one ($M_p \geq 2.5 M_J$). The distributions shown as dashed lines were obtained using the

photoevaporation profile from Paper I, while the solid lines use the profiles obtained in this study.

There are qualitative similarities between the distributions obtained using the Paper I prescription and this work. Both populations predict an under-density of giant planets in the inner disc regions and a peak outside the gap opening regions. However, the position of the peaks and troughs is considerably different. The reason for this is that gap opening occurs earlier in these models (see Figure 6), thus allowing less time for the planets to migrate inwards before the surface density of the disc around them is depleted by the wind and they are ultimately parked.

We note that the populations presented here are not meant as a predictive tool to interpret exoplanet survey results. Unfortunately, the lack of a self-consistent planet formation formalism in our 1D code is a serious limitation to the predictive power of our models (cf. Monsch et al. 2021b, for a detailed discussion). However, this exercise is still useful to illustrate the sensitivities of 1D planet population synthesis approaches to the details of the disc dispersal prescription used.

5 CONCLUSIONS

We have presented a new set of input X-ray spectra from young stars that was derived from an emission measure analysis of observed T Tauri stars in the COUP survey. The spectra were used to produce new prescriptions of X-ray photoevaporation, which may be included into disc and planet population synthesis models. The spectra, which are included in the supplementary online data accompanying this paper, can also be used for studies of the irradiation of very young planetary atmospheres at the time of disc dispersal.

We show that the total mass loss rates (\dot{M}_w) are controlled by the luminosities in the soft X-ray band $L_{x,\text{soft}}$ (100 eV to 1 keV), and we provide a new relation allowing to scale \dot{M}_w by $L_{x,\text{soft}}$ (Eq. 9). In agreement with previous work presented in Paper I, we find that the total mass loss rates do not scale linearly with X-ray luminosity. At high X-ray luminosities the disc wind in the inner region becomes dense enough to screen the outer disc regions, thus limiting the growth of the total disc mass loss rate. This is reflected in the radial profile of the wind, which peaks closer in and does not extend as far for higher X-ray luminosities and harder spectra.

Furthermore, the new spectra are more luminous in the soft X-ray band, resulting in more vigorous wind mass loss rates for the same total X-ray luminosity, compared to the discs irradiated by the spectra presented in Paper I. This strongly affects the surface density evolution of the discs, resulting in a faster dispersal and opening of a gap in more massive discs.

The agreement between predicted and observed transition disc statistics moderately improved using the new spectra. However, the observed population of strongly accreting, large-cavity transition discs can still not be reproduced. Furthermore, the new models still over-predict the population of non-accreting transition discs. We suggest, however, that due to radial drift having depleted the outer disc of mm-sized grains, this non-accreting transition disc population

column density	a	b	c	d	m
5e20	1.5	-18.150	-7.856	3.973	0.278
1e21	1.5	-21.945	-6.861	3.935	0.269
1.5e21	1.5	-17.592	-6.503	3.919	0.357
2e21	1.5	-23.580	-6.154	3.882	0.322
2.5e21	1.5	-24.918	-6.018	3.920	0.268
3e21	1.5	-26.731	-5.644	3.903	0.306
3.5e21	1.5	-34.038	-5.420	3.893	0.271
4.e21	1.5	-26.362	-5.149	3.882	0.430
4.5e21	1.5	-28.736	-5.130	3.877	0.374
5e21	1.5	-22.981	-4.975	3.872	0.497
5.5e21	1.5	-16.510	-4.816	3.872	0.700
6e21	1.5	-16.000	-4.735	3.872	0.691
6.5e21	1.5	-16.000	-4.718	3.877	0.608
7e21	1.5	-16.000	-4.623	3.865	0.674
7.5e21	1.5	-16.000	-4.540	3.860	0.700
8e21	1.5	-16.637	-4.462	3.859	0.700
8.5e21	1.5	-16.772	-4.387	3.855	0.700
9e21	1.5	-16.246	-4.354	3.853	0.700
9.5e21	1.5	-16.000	-4.362	3.851	0.686
1e22	1.5	-22.027	-4.446	3.841	0.477
1.05e22	1.5	-18.575	-4.364	3.845	0.572
1.1e22	1.5	-17.397	-4.240	3.835	0.692
1.15e22	1.5	-17.616	-4.219	3.823	0.700
1.2e22	1.5	-16.000	-4.270	3.832	0.647
1.25e22	1.5	-17.137	-4.251	3.846	0.700
1.3e22	1.5	-29.908	-4.730	3.624	0.417
1.35e22	1.5	-44.599	-4.702	3.625	0.280
1.4e22	1.5	-45.048	-4.624	3.620	0.331
1.45e22	1.5	-31.371	-4.606	3.617	0.455
1.5e22	1.5	-24.526	-4.553	3.629	0.559
1.55e22	1.5	-37.325	-4.536	3.621	0.411
1.6e22	1.5	-100.000	-4.558	3.619	0.155
1.65e22	1.5	-27.527	-4.459	3.615	0.555
1.7e22	1.5	-100.000	-4.540	3.625	0.133
1.75e22	1.5	-21.203	-4.374	3.634	0.700
1.8e22	1.5	-21.639	-4.344	3.628	0.700
1.85e22	1.5	-100.000	-4.552	3.634	0.118
1.9e22	1.5	-100.000	-4.565	3.628	0.111
1.95e22	1.5	-31.118	-4.328	3.629	0.512
2e22	1.5	-58.579	-4.472	3.639	0.210

Table A1. Parameters for the temperature prescription in equation 1 for the $\log L_X = 29$ spectra.

column density	a	b	c	d	m
5e20	1.6	-23.995	-7.704	3.960	0.217
1e21	1.6	-27.727	-6.859	3.927	0.210
1.5e21	1.6	-20.571	-6.430	3.908	0.306
2e21	1.6	-28.534	-6.047	3.864	0.279
2.5e21	1.6	-80.000	-5.840	3.906	0.089
3e21	1.6	-77.487	-5.473	3.874	0.124
3.5e21	1.6	-46.869	-5.184	3.868	0.239
4.e21	1.6	-74.470	-5.079	3.861	0.154
4.5e21	1.6	-25.499	-4.868	3.859	0.468
5e21	1.6	-24.746	-4.754	3.855	0.500
5.5e21	1.6	-20.763	-4.630	3.845	0.654
6e21	1.6	-20.190	-4.621	3.847	0.604
6.5e21	1.6	-18.177	-4.501	3.836	0.750
7e21	1.6	-17.636	-4.415	3.840	0.750
7.5e21	1.6	-16.721	-4.413	3.843	0.750
8e21	1.6	-16.644	-4.349	3.844	0.750
8.5e21	1.6	-18.656	-4.303	3.829	0.750
9e21	1.6	-16.721	-4.298	3.836	0.750
9.5e21	1.6	-17.576	-4.261	3.830	0.750
1e22	1.6	-16.000	-4.262	3.830	0.750
1.05e22	1.6	-16.000	-4.273	3.820	0.750
1.1e22	1.6	-16.000	-4.304	3.821	0.671
1.15e22	1.6	-16.000	-4.237	3.808	0.731
1.2e22	1.6	-16.000	-4.227	3.810	0.750
1.25e22	1.6	-20.873	-4.295	3.806	0.650
1.3e22	1.6	-80.000	-4.734	3.607	0.156
1.35e22	1.6	-21.333	-4.597	3.616	0.635
1.4e22	1.6	-22.201	-4.520	3.604	0.750
1.45e22	1.6	-20.889	-4.504	3.613	0.750
1.5e22	1.6	-17.737	-4.460	3.632	0.750
1.55e22	1.6	-16.000	-4.520	3.635	0.750
1.6e22	1.6	-16.000	-4.507	3.637	0.731
1.65e22	1.6	-16.000	-4.849	3.653	0.473
1.7e22	1.6	-16.000	-4.507	3.626	0.729
1.75e22	1.6	-16.000	-4.622	3.642	0.609
1.8e22	1.6	-16.000	-4.592	3.635	0.649
1.85e22	1.6	-16.000	-4.479	3.638	0.727
1.9e22	1.6	-16.000	-4.924	3.678	0.412
1.95e22	1.6	-80.000	-4.608	3.620	0.147
2e22	1.6	-22.005	-4.667	3.636	0.443

Table A2. Parameters for the temperature prescription in equation 1 for the $\log(L_X) = 30$ spectra.

may be difficult to observe, thus somewhat easing the tension between the model predictions and the observations.

Finally we show that simple planet population synthesis models are very sensitive to the choice of the disc dispersal prescription, which further motivates the development of accurate photoevaporative disc dispersal models.

6 DATA AVAILABILITY

The data underlying this article are available in the article and in its online supplementary material.

APPENDIX A: TEMPERATURE PRESCRIPTION

Tables A1, A2 and A3 list the parameters for the temperature prescription given in equation 1.

REFERENCES

- Alexander R., Pascucci I., Andrews S., Armitage P., Cieza L., 2014, in Beuther H., Klessen R. S., Dullemond C. P., Henning T., eds, *Protostars and Planets VI*. p. 475 ([arXiv:1311.1819](https://arxiv.org/abs/1311.1819)), [doi:10.2458/azu_uapress_9780816531240-ch021](https://doi.org/10.2458/azu_uapress_9780816531240-ch021)
- Armitage P. J., Livio M., Lubow S. H., Pringle J. E., 2002, *MNRAS*, **334**, 248
- Banzatti A., Pascucci I., Edwards S., Fang M., Gorti U., Flock M., 2019, *ApJ*, **870**, 76
- Clarke C. J., Gendrin A., Sotomayor M., 2001, *MNRAS*, **328**, 485
- D'Alessio P., Calvet N., Hartmann L., 2001, *The Astrophysical Journal*, **553**, 321
- Ercolano B., Clarke C. J., 2010, *Monthly Notices of the Royal Astronomical Society*, **402**, 2735
- Ercolano B., Owen J. E., 2010, *MNRAS*, **406**, 1553
- Ercolano B., Owen J. E., 2016, *MNRAS*, **460**, 3472
- Ercolano B., Pascucci I., 2017a, *Royal Society Open Science*, **4**, 170114

column density	a	b	c	d	m
5e20	1.7	-99.660	-8.590	3.954	0.044
1e21	1.7	-44.297	-7.498	3.884	0.141
1.5e21	1.7	-23.265	-6.982	3.857	0.329
2e21	1.7	-18.870	-6.805	3.860	0.400
2.5e21	1.7	-16.173	-6.734	3.879	0.400
3e21	1.7	-14.544	-6.648	3.888	0.400
3.5e21	1.7	-17.330	-6.676	3.883	0.314
4.e21	1.7	-23.577	-6.605	3.898	0.215
4.5e21	1.7	-28.298	-6.450	3.884	0.191
5e21	1.7	-38.879	-6.317	3.865	0.151
5.5e21	1.7	-31.700	-6.342	3.860	0.176
6e21	1.7	-22.163	-6.218	3.843	0.281
6.5e21	1.7	-22.438	-6.270	3.845	0.256
7e21	1.7	-36.034	-6.212	3.838	0.162
7.5e21	1.7	-30.500	-6.203	3.831	0.193
8e21	1.7	-47.757	-6.138	3.814	0.132
8.5e21	1.7	-35.389	-6.131	3.834	0.159
9e21	1.7	-32.633	-6.093	3.828	0.177
9.5e21	1.7	-24.455	-5.991	3.812	0.260
1e22	1.7	-24.433	-6.035	3.811	0.247
1.05e22	1.7	-21.125	-5.995	3.807	0.290
1.1e22	1.7	-30.889	-6.083	3.808	0.178
1.15e22	1.7	-28.621	-6.019	3.809	0.201
1.2e22	1.7	-35.809	-5.997	3.795	0.171
1.25e22	1.7	-24.734	-5.910	3.805	0.259
1.3e22	1.7	-15.639	-5.866	3.767	0.500
1.35e22	1.7	-14.278	-5.932	3.765	0.500
1.4e22	1.7	-14.057	-5.968	3.767	0.500
1.45e22	1.7	-13.756	-5.996	3.771	0.500
1.5e22	1.7	-14.176	-5.946	3.760	0.500
1.55e22	1.7	-13.987	-5.950	3.770	0.500
1.6e22	1.7	-13.770	-5.951	3.770	0.500
1.65e22	1.7	-13.806	-5.961	3.766	0.500
1.7e22	1.7	-13.944	-5.964	3.767	0.500
1.75e22	1.7	-12.973	-6.025	3.787	0.500
1.8e22	1.7	-12.469	-6.049	3.788	0.500
1.85e22	1.7	-13.872	-5.984	3.777	0.500
1.9e22	1.7	-14.485	-5.938	3.779	0.500
1.95e22	1.7	-14.530	-5.942	3.776	0.500
2e22	1.7	-14.535	-5.910	3.783	0.500

Table A3. Parameters for the temperature prescription in Eq. 1 for the log $L_X = 31$ spectra.

- Ercolano B., Pascucci I., 2017b, [Royal Society Open Science](#), 4, 170114
- Ercolano B., Rosotti G., 2015, [MNRAS](#), 450, 3008
- Ercolano B., Barlow M. J., Storey P. J., Liu X. W., 2003, [MNRAS](#), 340, 1136
- Ercolano B., Barlow M. J., Storey P. J., 2005, [MNRAS](#), 362, 1038
- Ercolano B., Young P. R., Drake J. J., Raymond J. C., 2008a, [ApJS](#), 175, 534
- Ercolano B., Drake J. J., Raymond J. C., Clarke C. C., 2008b, [ApJ](#), 688, 398
- Ercolano B., Drake J. J., Raymond J. C., Clarke C. C., 2008c, [ApJ](#), 688, 398
- Ercolano B., Clarke C. J., Drake J. J., 2009a, [ApJ](#), 699, 1639
- Ercolano B., Clarke C. J., Drake J. J., 2009b, [ApJ](#), 699, 1639
- Ercolano B., Clarke C. J., Hall A. C., 2011, [MNRAS](#), 410, 671
- Ercolano B., Mayr D., Owen J. E., Rosotti G., Manara C. F., 2014, [MNRAS](#), 439, 256
- Ercolano B., Koepferl C., Owen J., Robitaille T., 2015, [MNRAS](#), 452, 3689
- Ercolano B., Jennings J., Rosotti G., Birnstiel T., 2017, [MNRAS](#), 472, 4117
- Ercolano B., Weber M. L., Owen J. E., 2018, [MNRAS](#), 473, L64
- Flaischlen S., Preibisch T., Manara C. F., Ercolano B., 2021, [A&A](#), 648, A121
- Gangi M., et al., 2020, [A&A](#), 643, A32
- Getman K. V., et al., 2005, [ApJS](#), 160, 319
- Jennings J., Ercolano B., Rosotti G. P., 2018, [MNRAS](#), 477, 4131
- Kashyap V., Drake J. J., 2000, [Bulletin of the Astronomical Society of India](#), 28, 475
- Koepferl C. M., Ercolano B., Dale J., Teixeira P. S., Ratzka T., Spezzi L., 2013, [MNRAS](#), 428, 3327
- Kunitomo M., Suzuki T. K., Inutsuka S.-i., 2020, [MNRAS](#), 492, 3849
- Lin D. N. C., Papaloizou J., 1979, [MNRAS](#), 186, 799
- Lin D. N. C., Papaloizou J., 1986, [ApJ](#), 309, 846
- Luhman K. L., Allen P. R., Espaillat C., Hartmann L., Calvet N., 2010, [ApJS](#), 186, 111
- Lynden-Bell D., Pringle J. E., 1974, [MNRAS](#), 168, 603
- Manara C. F., Mordasini C., Testi L., Williams J. P., Miotello A., Lodato G., Emsenhuber A., 2019, [A&A](#), 631, L2
- Mignone A., Bodo G., Massaglia S., Matsakos T., Tesileanu O., Zanni C., Ferrari A., 2007, [The Astrophysical Journal Supplement Series](#), 170, 228
- Monsch K., Ercolano B., Picogna G., Preibisch T., Rau M. M., 2019, [MNRAS](#), 483, 3448
- Monsch K., Picogna G., Ercolano B., Kley W., 2021a, [arXiv e-prints](#), p. [arXiv:2101.01179](#)
- Monsch K., Picogna G., Ercolano B., Preibisch T., 2021b, [arXiv e-prints](#), p. [arXiv:2105.05908](#)
- Nakatani R., Hosokawa T., Yoshida N., Nomura H., Kuiper R., 2018, [ApJ](#), 865, 75
- Nisini B., Antonucci S., Alcalá J. M., Giannini T., Manara C. F., Natta A., Fedele D., Biazzo K., 2018, [A&A](#), 609, A87
- Owen J. E., Ercolano B., Clarke C. J., Alexander R. D., 2010, [Monthly Notices of the Royal Astronomical Society](#), 401, 1415
- Owen J. E., Ercolano B., Clarke C. J., 2011, [Monthly Notices of the Royal Astronomical Society](#), 412, 13
- Owen J. E., Clarke C. J., Ercolano B., 2012, [Monthly Notices of the Royal Astronomical Society](#), 422, 1880
- Pascucci I., et al., 2020, [ApJ](#), 903, 78
- Picogna G., Ercolano B., Owen J. E., Weber M. L., 2019, [MNRAS](#), 487, 691
- Pollack J. B., Hubickyj O., Bodenheimer P., Lissauer J. J., Podolak M., Greenzweig Y., 1996, [Icarus](#), 124, 62
- Preibisch T., et al., 2005, [ApJS](#), 160, 401
- Ribas Á., Merín B., Bouy H., Maud L. T., 2014, [A&A](#), 561, A54
- Ribas Á., Bouy H., Merín B., 2015, [A&A](#), 576, A52
- Ruden S. P., 2004, [ApJ](#), 605, 880
- Schisano E., Ercolano B., Güdel M., 2010, [MNRAS](#), 401, 1636
- Shakura N. I., Sunyaev R. A., 1973, [A&A](#), 500, 33
- Wang L., Goodman J. J., 2017a, [ApJ](#), 835, 59

- Wang L., Goodman J., 2017b, [ApJ](#), **847**, 11
Weber M. L., Ercolano B., Picogna G., Hartmann L., Rodenkirch P. J., 2020, [MNRAS](#), **496**, 223
Wölfer L., Picogna G., Ercolano B., van Dishoeck E. F., 2019, [MNRAS](#), **490**, 5596

ACKNOWLEDGEMENTS

We thank the anonymous referee for a detailed and constructive report which helped improve our manuscript. We acknowledge the support of the DFG priority program SPP 1992 “Exploring the Diversity of Extrasolar Planets” (DFG PR 569/13-1, ER 685/7-1) & the DFG Research Unit “Transition discs” (FOR 2634/1, ER 685/8-2). This research was supported by the Excellence Cluster ORIGINS which is funded by the Deutsche Forschungsgemeinschaft (DFG, German Research Foundation) under Germany’s Excellence Strategy - EXC-2094 - 390783311. The simulations have been partly carried out on the computing facilities of the Computational Center for Particle and Astrophysics (C2PAP). JJD was funded by NASA contract NAS8-03060 to the *Chandra* X-ray Center and thanks the Director, Pat Slane, and the CXC science team for continuing advice and support.